
Application of in-situ process monitoring to optimise laser processing parameters during the powder bed fusion printing of Ti-6Al-4V

John J. Power¹, Mark Hartnett², & Denis P. Dowling¹

¹I-Form Centre, School of Mechanical and Materials Engineering, University College Dublin, Dublin, D04 V1W8, Belfield, Ireland

²Irish Manufacturing Research, Block A, Collegelands, Rathcoole, Co. Dublin, D24 WC04, Ireland

john.power1@ucdconnect.ie

Abstract

This study evaluates the use of in-situ process monitoring feedback as an approach to help reduce print defects such as porosity, during the laser powder bed fusion (L-PBF) of Ti-6Al-4V overhang structures. During initial printing trials it was observed in the region around the print overhang structure that increased porosity levels were present with a volume fraction of up to 0.08% compared with <0.02% in the bulk alloy. It is hypothesized that the increased porosity is associated with the excess heat generated in the overhang region due to the decreased thermal conductivity of the unmelted powder beneath the print layers compared with the solid alloy. Additionally, excess porosity and inclusions were observed in the regions adjacent to the overhang melt pool and attributed to spatter ejection from the overhang melt pool. In-situ process monitoring data obtained from the melt pool infrared emissions was correlated with the properties of the printed parts. This in-process data was then used to assist in selecting optimal laser processing conditions to prevent the melt pool from overheating at the overhang region. By systematically controlling the laser energy while printing the first fifteen layers over the overhang structure, the bulk alloy's porosity level was reduced to <0.02%. There was also an associated reduction in the roughness (Ra) of the overhang itself, with its Ra decreasing from 62.4±7.3 to 7.5±1.9 µm.

Laser powder bed fusion, In-situ process monitoring, Titanium, Porosity, Roughness

1. Introduction

Additive manufacturing (AM) can create complex geometries and features that conventional formative and subtractive manufacturing cannot readily produce. For this reason, AM has seen an increased use in the biomedical [1] and aerospace sectors [2]. However, one of the critical limitations of AM is the ability to control the level of porosity [3] and the as-built surface quality of printed parts [4].

Examples of porosity defects in Ti-6Al-4V alloy parts fabricated using L-PBF include lack of fusion (LOF) and keyhole (KH) [3]. Incomplete melting of the powder due to rapid scanning speeds or low power can result in small irregularly shaped pores, referred to as LOF pores. In contrast, excessive laser power or slower scanning speeds can cause KH pore formation, vaporising the material in the melt pool. This vapour is trapped in the resolidifying alloy, resulting in bubble-like cavities after solidification [5]. This over-melting of the powder bed significantly affects the incorporation of unmelted powder, leading to the formation of voids and porosity.

Relatively high roughness levels observed at the downskin or overhang surfaces of L-PBF parts are another common print defect [6, 7]. Several print parameters can affect the formation of rough surfaces, including laser power and scanning speed [8, 9]. Excess heat in the liquid melt pool can cause surface tension gradient-driven flow inside the melt pool, known as Marangoni convection. This Marangoni convection can lead to instability in the melt pool and affect the shape and formation of the downskin surfaces.

Overhang surfaces challenge the capabilities of the L-PBF process in terms of heat distribution [10] and control over melt pool dynamics [11]. The adverse defects observed in overhang

structures fabricated using LPBF are thought to be induced by the difference in absorbed energy into the melt pool at the powder-supported zone versus the solid-supported zone. In-situ process monitoring has seen increased use with the L-PBF process. It can detect defects, including those associated with overhang structures. Optical emission spectroscopy and thermal monitoring are among the in-process monitoring techniques used to monitor L-PBF printing [12-17]. These in situ techniques have also been used by a small number of authors to investigate the laser melt pool during the printing of overhang structures [11, 14, 18]. For example, Egan et al. [14] used process monitoring data obtained from an in situ optical emission spectroscopy setup during L-PBF printing (Renishaw RenAM 500M) to monitor the processing of the first layer printed above an internal cavity. Compared to the solid alloy, the poor thermal conductivity of the alloy powder resulted in an increased melt pool size and temperature. This increased temperature, arising from a decrease in thermal conduction away from a melt pool generated in an overhang, may have resulted in larger thermal gradients, which can, in turn, destabilize the melt pool.

As detailed above, the challenges of fabricating parts with overhangs are well documented in the literature. There have been limited studies on optimising processing parameters for overhang structure printing. The objective of this study is to establish the effects of the overheating that occurs at overhang layers compared to the bulk Ti-6Al-4V alloy. This evaluation will be based on comparing the changes in porosity and roughness. Additionally, the use of in-situ process monitoring to help select optimal processing parameters for overhang structures will be investigated. The goal is to achieve a higher level of homogeneity between the porosity and roughness in the regions around the overhang and the bulk Ti-6Al-4V.

2. Materials and methods

2.1. Materials and processing parameters

Extra-low interstitial Ti-6Al-4V (Grade 23, ELI-0406) powder, with particle size in the 10–45 μm range, was sourced from Renishaw Plc [19]. This printing study was conducted on a Renishaw RenAM 500M system operating under an inert gas atmosphere. Additionally, this AM system has an in situ processing monitoring (PM) system called InfnAM Spectral [20]. The latter system uses several photodiodes to gather data relating to the thermal and optical emissions (in the near-infrared range) from the laser melt pool created during the build process and provide feedback on the laser energy output from the machine [21].

As the objective of this study was to evaluate if in-process monitoring could be used to select optimised process parameters for the printing of overhang structures, the Ti-6Al-4V test sample was designed to simulate a flat overhang structure. Figure 1 shows the design of the test piece used in this study, with the overhang region highlighted by dashed lines in the plan and side view of the drawing schematic.

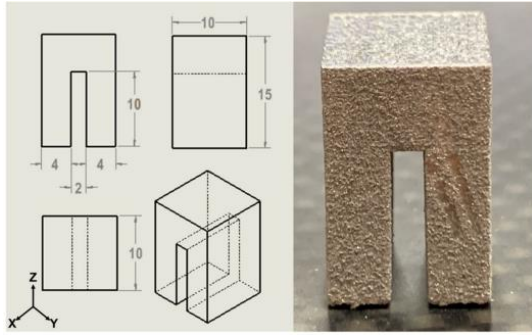


Figure 1. Overhang test piece: **left** design and dimensions (in mm) and **right** photograph of the printed Ti-6Al-4V alloy part.

Table 1: Processing conditions investigated. Detailed are the percentage reductions in laser power and the exposure time reduction, which indicates the percentage change between subsequent layers until parameters are returned to nominal levels. Also included are the number of layers the laser processing parameters were altered. The average VED column indicates the overall level of laser energy reduction.

Test Condition	Power Reduction (%)	Exposure Time Reduction (%)	No. of gradient layers	Average VED for the 15 layers above overhang (J/mm^3)
1	12.5	5	1	67.6
2	5	12.5	1	67.6
3	5	20	1	67.3
4	20	5	1	67.3
5	20	20	1	66.7
6	20	20	8	39.8
7	5	5	8	55.5
8	12.5	12.5	8	45.0
9	20	5	15	14.2
10	12.5	20	15	10.6
11	5	5	15	33.1
12	20	12.5	15	10.6
13	5	20	15	14.2

The first overhang layer was deposited directly onto the unconsolidated powder material below without part supports after 10 mm (464 layers) of powder material had been deposited and melted to form the solid leg structures. The overhang area of the test piece was 2×10 mm. For non-overhang regions, a laser power of 200 W, exposure time of 50 μs and a modulated 10 ms delay between exposures was used, as recommended by the printer manufacturer for Ti-6Al-4V alloy. For the overhang region, these parameters varied, as detailed in the next section. The alloy samples were built using a pulse laser mode with a 65

μm hatch distance using a meander zigzag scan strategy, rotated 67° degrees between each layer, a spot size of 80 μm , layer thickness of 30 μm , and point distance of 75 μm . The delay time between each recoating of the powder was approximately 30 s, and a gas flow rate (Ar) of roughly 29 m^3/h was used during printing.

2.2. In-situ process monitoring data analysis

A series of experiments was proposed to help identify the processing conditions which would yield a more homogeneous overhang melt pool temperature profile comparable with that obtained within the bulk alloy. A Box-Behnken design was used to alter three parameters: the laser power and laser exposure time in steps of 5.0%, 12.5%, or 20.0% in either one, eight, or fifteen layers above the overhang. For example, test condition 6 involved a laser power reduction of 5% over eight layers. This involved printing the first overhang layer with 66% of the laser power (133W), which was used to print the bulk alloy. Each subsequent layer was then printed with an increase of laser power of 5% from the previous layer until the laser power reached nominal laser power (200W). The parameter changes are only applied to melt tracks printed directly onto the 2×10 mm overhang region in the centre of the part after layer 464 for one, eight, or fifteen layers. The approach resulted in thirteen print experiments, with three replicants: in all, thirty-nine overhang samples were printed and investigated, as detailed in Table 1. Each sample's volumetric energy density (VED) was calculated using Eq. 1 [22].

$$VED = \frac{Pe_t}{hd_p d_h} \left[\frac{\text{J}}{\text{mm}^3} \right]$$

Equation 1: Volumetric energy density formula for parts printed using modulated wave laser [22].

Where P (W) is the laser power, e_t (μs) is the laser exposure time, h (μm) is the layer thickness, d_p (μm) is the point distance, and d_h (μm) is the hatching distance. The VED for the non-overhang regions of the build was calculated as 68.4 J/mm^3 . Table 1 details the average VED for the overhang region over fifteen layers above the overhang.

To evaluate the success of each set of processing conditions, the melt pool emissions in the overhang regions were compared with those in the non-overhang regions in the same print layer. This was done by comparing the in-process monitoring IR

photodiode readings. The pixel intensity associated with each part measured using the PM software was obtained by taking images of the 2D reconstructions of each layer and analysing them using ImageJ software. This analysis of the IR emission data allowed for samples that had not experienced overheating at the overhang to be identified. The in situ data was then correlated with the overhang roughness and porosity data obtained for each print sample.

2.3. Porosity and roughness measurements

Part porosity was evaluated using a GE Phoenix Nanotom M microcomputed tomography (μ CT) system, operating at 150 kV and 200 μ m, with a scan time of approximately 10 minutes [23]. The resolution of each scan was 12 μ m, defined as the smallest detectable pore size in the sample. The μ CT scans were analysed using the porosity/inclusion analysis (PLA) module in VGStudio Max version 3.5 [24]. Optical microscopy (OM) was also carried out using an Olympus GX51 optical microscope at 10x magnification. The size and shape of pores at the overhang surface were analysed to determine the type of porosity present. Porosity was evaluated in the solidified alloy directly above the overhang and in the entire structure to compare the effect the overhang had on porosity formation.

Overhang roughness measurements were obtained based on the μ CT measurements using an approach previously applied to AM-printed porous structures [25]. The roughness of the overhanging edge was determined based on the profile lines taken from 2D cross-sectional images of the overhang. The overhang profile line was extracted using an ImageJ script written by the first author. This script analyses the pixels along the overhanging edge within a user-selected region of interest. It measures the edge roughness in correspondence with ISO 21920-2:2021. The average roughness (R_a) was determined for each test sample using Eq. 2. Five measurements were taken from five different cross-sections of each sample.

$$R_a = \frac{1}{l_e} \int_0^{l_e} |z(x)| dx$$

Equation 2: The arithmetic mean of the absolute values of the ordinate values [26].

3. Results and discussion

The objective of this study is to identify the laser processing conditions that minimized the measured porosity and roughness. Assessment of overheating in the overhang region is based on photodiode intensity measurements. The Ti-6Al-4V overhang samples printed using the processing conditions detailed in Table 1 were cross-sectioned, mounted, ground, polished, and examined using optical microscopy. LOF porosity large irregular pores with sharp corners and edges, was present in samples where insufficient fusion of metal powder occurred. The presence of LOF pores highlights that simply reducing the level of laser energy used to print the overhang can result in different defect types, compared with those obtained when excess laser energy is used.

Keyhole pores formed in the layers closer to the powder bed in each sample. The poor thermal conductance of the powder bed below the overhang and the initial layers deposited onto the powder bed to form the overhang would have led to an increase in the local melt pool temperature, increasing the chance of material vaporization and keyhole formation. Keyhole porosity was the most common type of porosity observed in samples printed with a higher laser energy.

Increased porosity was observed in the print layers immediately above the overhang, up to 0.08% volume fraction.

This was substantially higher than the level of porosity observed in the bulk alloy regions, which averaged less than 0.02% for all samples. Samples printed with lower laser energy density (test conditions 6, 9, 10, 12, and 13) exhibited higher levels of porosity. This was attributed to pore formation in the area laterally of the overhang regions, figure 2, likely due to spatter ejection from the unstable melt pool [27].

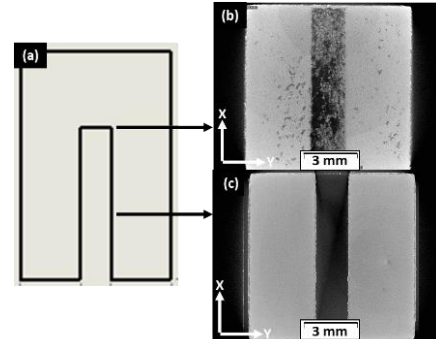


Figure 2. (a) Schematic showing the front view of the overhang test piece. The arrows indicate the approximate location of the layer views from the μ CT scans shown. (b) μ CT scan images showing the first overhang print layer (layer 464) with an increased level of porosity visible (dark patches) in the non-overhang regions of the part. (c) μ CT scan showing print layer (layer 250) which was located away from the overhang and exhibited no visible porosity.

Figure 3 shows the R_a roughness measurement for test samples along with the average IR photodiode measurement for the overhang melt pools. This demonstrated a broad correlation between the intensity of the laser energy used to print the sample and the (R_a) roughness measurements obtained from the CT scans. This figure also includes the associated photodiode measurements. When higher photodiode measurements were recorded, associated with higher melt pool energy, there was generally an associated increase in roughness. However, this correlation was not observed for all overhang samples, e.g. sample 11. A reduction in laser power, and therefore melt pool temperature, has previously been linked to reduced surface roughness [4].

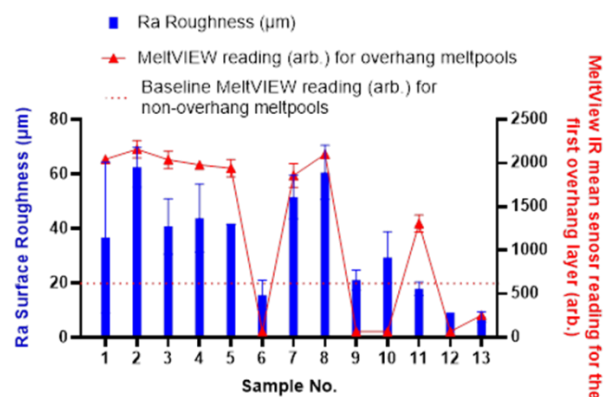


Figure 3. R_a roughness of overhang surface graphed with the average IR photodiode sensor reading (arb.) for the first overhang layer melt pool.

4. Conclusions

Overhang structures in printed alloy structures can create difficulties due to variations in the melt pool temperature, due to decreased thermal conductivity of the powder immediately below the printed overhang layers. In this study a design of experiments was carried out and the results were in-formed

based on in-process monitoring (photodiode measurements) of the melt pool temperature. By tailoring the laser processing conditions for the first 15 layers over the overhang localised overheating was minimised. The level of porosity was significantly reduced. Porosity levels (volume fraction) of up to 0.08% in the overhang region were reduced to the <0.02% obtained for the bulk alloy. There was an associated reduction of up to 88% in the roughness (Ra) of the overhang itself.

References

- [1] L. E. Murr *et al.*, "Microstructure and mechanical behavior of Ti-6Al-4V produced by rapid-layer manufacturing, for biomedical applications," *Journal of the Mechanical Behavior of Biomedical Materials*, vol. 2, no. 1, pp. 20-32, 2009/01/01/ 2009, doi: <https://doi.org/10.1016/j.imbbm.2008.05.004>.
- [2] R. Liu, Z. Wang, T. Sparks, F. Liou, and J. Newkirk, "13 - Aerospace applications of laser additive manufacturing," in *Laser Additive Manufacturing*, M. Brandt Ed.: Woodhead Publishing, 2017, pp. 351-371.
- [3] H. Gong, K. Rafi, H. Gu, T. Starr, and B. Stucker, "Analysis of defect generation in Ti-6Al-4V parts made using powder bed fusion additive manufacturing processes," *Additive Manufacturing*, vol. 1, pp. 87-98, 2014.
- [4] J. C. Fox, S. P. Moylan, and B. M. Lane, "Effect of Process Parameters on the Surface Roughness of Overhanging Structures in Laser Powder Bed Fusion Additive Manufacturing," *Procedia CIRP*, vol. 45, pp. 131-134, 2016/01/01/ 2016, doi: <https://doi.org/10.1016/j.procir.2016.02.347>.
- [5] G. Kasperovich, J. Haubrich, J. Gussone, and G. Requena, "Correlation between porosity and processing parameters in TiAl6V4 produced by selective laser melting," *Materials & Design*, vol. 105, pp. 160-170, 2016.
- [6] S. Rahmati and E. Vahabli, "Evaluation of analytical modeling for improvement of surface roughness of FDM test part using measurement results," *The International Journal of Advanced Manufacturing Technology*, vol. 79, no. 5, pp. 823-829, 2015.
- [7] C. Qiu, C. Panwisawas, M. Ward, H. C. Basoalto, J. W. Brooks, and M. M. Attallah, "On the role of melt flow into the surface structure and porosity development during selective laser melting," *Acta Materialia*, vol. 96, pp. 72-79, 2015.
- [8] J. Gockel, L. Sheridan, B. Koerper, and B. Whip, "The influence of additive manufacturing processing parameters on surface roughness and fatigue life," *International Journal of Fatigue*, vol. 124, pp. 380-388, 2019/07/01/ 2019, doi: <https://doi.org/10.1016/j.ijfatigue.2019.03.025>.
- [9] D. Wang, Y. Yang, Z. Yi, and X. Su, "Research on the fabricating quality optimization of the overhanging surface in SLM process," *The International Journal of Advanced Manufacturing Technology*, vol. 65, no. 9, pp. 1471-1484, 2013.
- [10] A. Ashby *et al.*, "Thermal history and high-speed optical imaging of overhang structures during laser powder bed fusion: A computational and experimental analysis," *Additive Manufacturing*, vol. 53, p. 102669, 2022/05/01/ 2022, doi: <https://doi.org/10.1016/j.addma.2022.102669>.
- [11] Q. Han, H. Gu, S. Soe, R. Setchi, F. Lacan, and J. Hill, "Manufacturability of AlSi10Mg overhang structures fabricated by laser powder bed fusion," *Materials & Design*, vol. 160, pp. 1080-1095, 2018/12/15/ 2018, doi: <https://doi.org/10.1016/j.matdes.2018.10.043>.
- [12] S. Clijsters, T. Craeghs, S. Buls, K. Kempen, and J.-P. Kruth, "In situ quality control of the selective laser melting process using a high-speed, real-time melt pool monitoring system," *The International Journal of Advanced Manufacturing Technology*, vol. 75, pp. 1089-1101, 2014.
- [13] T. Craeghs, S. Clijsters, J. P. Kruth, F. Bechmann, and M. C. Ebert, "Detection of Process Failures in Layerwise Laser Melting with Optical Process Monitoring," *Physics Procedia*, vol. 39, pp. 753-759, 2012/01/01/ 2012, doi: <https://doi.org/10.1016/j.phpro.2012.10.097>.
- [14] D. S. Egan, K. Jones, and D. P. Dowling, "Selective laser melting of Ti-6Al-4V: Comparing μ CT with in-situ process monitoring data," *CIRP Journal of Manufacturing Science and Technology*, vol. 31, pp. 91-98, 2020/11/01/ 2020, doi: <https://doi.org/10.1016/j.cirpj.2020.10.004>.
- [15] C. S. Lough *et al.*, "Local prediction of Laser Powder Bed Fusion porosity by short-wave infrared imaging thermal feature porosity probability maps," *Journal of Materials Processing Technology*, vol. 302, p. 117473, 2022/04/01/ 2022, doi: <https://doi.org/10.1016/j.jimatprotec.2021.117473>.
- [16] D. Alberts, D. Schwarze, and G. Witt, "In situ melt pool monitoring and the correlation to part density of Inconel® 718 for quality assurance in selective laser melting," in *2017 International Solid Freeform Fabrication Symposium*, 2017: University of Texas at Austin.
- [17] S. Berumen, F. Bechmann, S. Lindner, J.-P. Kruth, and T. Craeghs, "Quality control of laser-and powder bed-based Additive Manufacturing (AM) technologies," *Physics procedia*, vol. 5, pp. 617-622, 2010.
- [18] L. Scime and J. Beuth, "Using machine learning to identify in-situ melt pool signatures indicative of flaw formation in a laser powder bed fusion additive manufacturing process," *Additive Manufacturing*, vol. 25, pp. 151-165, 2019/01/01/ 2019, doi: <https://doi.org/10.1016/j.addma.2018.11.010>.
- [19] Renishaw-PLC. "Ti6Al4V ELI-0406 powder for additive manufacturing." Renishaw PLC. <https://shorturl.at/bJQW9> (accessed Jan 10th, 2023).
- [20] Renishaw-PLC, "InfiniAM Spectral - Energy Input and Melt Pool Emissions Monitoring for AM Systems," 2017.
- [21] D. S. Egan and D. P. Dowling, "Correlating in-situ process monitoring data with the reduction in load bearing capacity of selective laser melted Ti-6Al-4V porous biomaterials," *Journal of the Mechanical Behavior of Biomedical Materials*, vol. 106, p. 103723, 2020.
- [22] G. Repossini, V. Laguzza, M. Grasso, and B. M. Colosimo, "On the use of spatter signature for in-situ monitoring of Laser Powder Bed Fusion," *Additive Manufacturing*, vol. 16, pp. 35-48, 2017.
- [23] "Phoenix Nanotom M 180 kV / 20 W X-ray nanoCT® system for high-resolution analysis and 3D metrology," ed. Cincinnati, Ohio, 2021.
- [24] VGStudio, "VGStudio Max 2.2 Reference Manual," ed. Heidelberg, Germany: VGStudio, 2012.
- [25] G. Kerckhofs, G. Pyka, M. Moesen, J. Schrooten, and M. Wevers, "High-resolution micro-CT as a tool for 3D surface roughness measurement of 3D additive manufactured porous structures," in *Proc ICT*, 2012, pp. 77-83.
- [26] *ISO 21920-2:2021 Geometrical product specifications (GPS) - Surface texture: Profile - Part 2: Terms, definitions and surface texture parameters*. Geneva: International Organization for Standardization, 2021.
- [27] S. Keaveney, A. Shmeliov, V. Nicolosi, and D. P. Dowling, "Investigation of process by-products during the Selective Laser Melting of Ti6AL4V powder," *Additive Manufacturing*, vol. 36, p. 101514, 2020/12/01/ 2020, doi: <https://doi.org/10.1016/j.addma.2020.101514>.